IOP Publishing New J. Phys. 26 (2024) 123008 https://doi.org/10.1088/1367-2630/ad9859

New Journal of Physics
The open access journal at the forefront of physics

Deutsche Physikalische Gesellschaft DPG
IOP Institute of Physics

Published in partnership with: Deutsche Physikalische Gesellschaft and the Institute of Physics

OPEN ACCESS

RECEIVED
23 July 2024

REVISED
1 November 2024

ACCEPTED FOR PUBLICATION
28 November 2024

PUBLISHED
9 December 2024

PAPER

Defect interactions in the non-reciprocal Cahn–Hilliard model

Navdeep Rana[1] and Ramin Golestanian[1,2,*]

[1] Max Planck Institute for Dynamics and Self-Organization (MPI-DS), D-37077 Göttingen, Germany
[2] Rudolf Peierls Centre for Theoretical Physics, University of Oxford, Oxford OX1 3PU, United Kingdom
[*] Author to whom any correspondence should be addressed.

E-mail: ramin.golestanian@ds.mpg.de

Keywords: defects, active matter, non-reciprocal interactions, pattern formation

Supplementary material for this article is available online

Abstract

We present a computational study of the pairwise interactions between defects in the recently introduced non-reciprocal Cahn–Hilliard model. The evolution of a defect pair exhibits dependence upon their corresponding topological charges, initial separation, and the non-reciprocity coupling constant α. We find that the stability of isolated topologically neutral targets significantly affects the pairwise defect interactions. At large separations, defect interactions are small and a defect pair is stable. When positioned in relatively close proximity, a pair of oppositely charged spirals or targets merge to form a single target. At low α, like-charged spirals form rotating bound pairs, which are however torn apart by spontaneously formed targets at high α. Similar preference for charged or neutral solutions is also seen for a spiral target pair where the spiral dominates at low α, but concedes to the target at large α. Our work sheds light on the complex phenomenology of non-reciprocal active matter systems when their collective dynamics involves topological defects.

1. Introduction

In the world of living and active matter, non-reciprocal interactions are the norm rather than the exception [1–6]. Interactions among active individuals, biological or synthetic, can arise from a variety of complex mechanisms, for example, chemical [1, 2], visual [7], social [8–10], programmable [6, 11], and wake-mediated [12]. The effective breaking of action-reaction symmetry gives rise to interesting phenomena, otherwise absent at thermal equilibrium, such as, self-propulsion in chemically active mixtures, both at micro and macroscopic scales [1, 2], and buckling instabilities in polar flocks [13]. In the non-reciprocal Cahn–Hilliard model (NRCH) [3–5, 14], parity and time-reversal (PT) symmetries break spontaneously. A variety of non-equilibrium features emerge, for example formation of travelling density bands [3, 4], suppression of coarsening [3, 15], and localized states [16]. A variant of the NRCH model with non-linear non-reciprocal interactions exhibits chaotic steady states where PT symmetry is locally restored in fluctuating domains [5]. Non-reciprocal interactions thus provide a generic mechanism that gives rise to wave propagation and the emergence of global polar order in active systems. NRCH model also emerges as a universal amplitude equation from the onset of a conserved-Hopf instability, which occurs in systems with two conservation laws [17]. Moreover, a systematic coarse-graining of a microscopic model of phoretically active Janus colloids [18] also results in a similar phenomenological description [19].

Topological defects play an important role in determining the dynamics of systems with broken symmetries [20], and have been extensively studied in the context of both equilibrium and non-equilibrium systems [21–24], as well as in quantum gases [25] and cosmology [26]. Defect unbinding drives the Berezinksii-Kosterlitz-Thouless transition at equilibrium [21, 27], and an analogous transition in active nematics [28], as well as coarsening dynamics of mixtures [29] and collective properties of type-II superconductors [30]. In models of ferromagnets [29, 31, 32], and Toner-Tu model of flocking [33, 34], coarsening proceeds via continuous merging of defects that exhibit (marginally) long-range interactions.

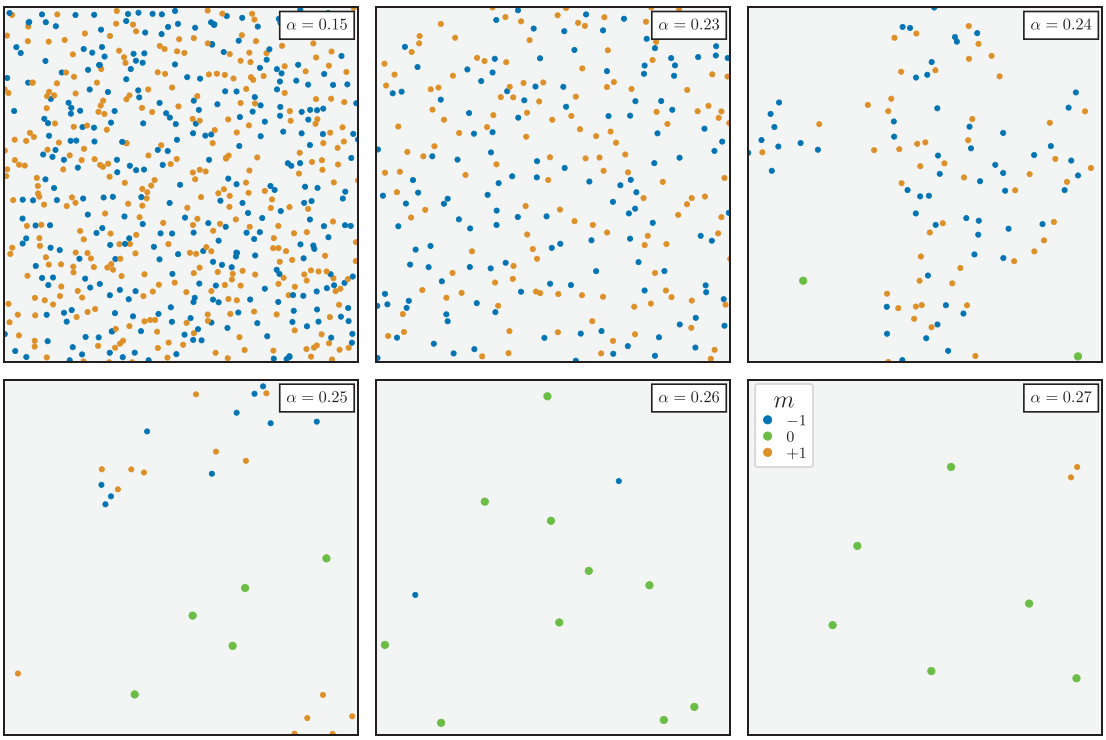

Figure 1. Distribution of spirals and targets identified by the locations of their cores for various values of α for a square of side $L = 6400$ discretized over $N = 4096$ collocation points in each direction. At small α, the defect networks are composed of isolated and bound pair of spirals. As we increase α, targets appear as well and are the dominant population of defects near α_c. Average inter-defect separation increases with α and targets show remarkably higher inter-defect separation as compared to the spirals.

Wet suspensions of polar active matter show spectacular defect-mediated flows, arising from the instabilities of the ordered states also known as active turbulence [35–41]. Furthermore, topological defects have been shown to play a key role in a wide range of phenomena in active matter [38, 39, 42–49].

There have been extensive studies in which defects have been used as fundamental singularities of the order parameter and effective theories have been developed in terms of the dynamics of the defects [50–68], including recent related developments in active matter [28, 69–76]. In the case of the complex Ginzburg-Landau (CGL) equation, defect cores have been shown to be screened from outside perturbations, and therefore, defect-interactions become short-ranged; the interactions are independent of charge but can be attractive or repulsive depending on the parameters [77–79].

In Rana and Golestanian [14], we have studied the defect solutions of the NRCH model, and shown that it admits two types of defects: spirals, which have a unit magnitude topological charge, and topologically neutral targets. For a given strength of non-reciprocity coupling α, defect solutions with a unique asymptotic wave number, $k_\infty \propto \sqrt{\alpha}$ and amplitude $R_\infty = \sqrt{1 - k_\infty^2}$ are selected [14]. Wavenumber selection and the Eckhaus instability [14, 79] set a threshold of $\alpha_\times$ above which defect solutions cease to exist. However, our large-scale numerical simulations, which start from random disordered states, reveal a disorder-order transition at $\alpha_c \ll \alpha_\times$. Below α_c, a disordered state evolves into a quasi-stationary network of defects with vanishing global polar order. Above α_c, we find noisy travelling waves with long-lived fluctuations. The topological composition of the defect networks also changes with α. For $\alpha \ll \alpha_c$, spirals are exclusively selected, whereas for $\alpha \lesssim \alpha_c$ we primarily observe target networks (see figure 1).

In this paper, we present a detailed numerical investigation of the defect interactions in the NRCH model. Our main motivation is to characterize and explain the features of the observed networks of defects, which are essentially arrested configurations. While isolated defects remain stationary, bound pairs of like-charged spirals are seen to orbit around a common centre [14]. One can then expect that the interactions between defects may fall rapidly with increasing separation. Similar features are also observed for the CGL equation, where the defect interactions decay exponentially [77, 78, 80]. We study pairwise defect interactions and show that they can be used to determine the properties of the the defect networks. We now summarize our main results before presenting a detailed description of the work.

1.1. Summary of our results

We uncover the pairwise defect interactions in the NRCH model and find that they are fundamentally different from previously characterized interactions in non-equilibrium systems with non-conserved order parameter [78, 79]. In non-conserved systems, adequately separated spirals repel each other independently of their topological charge and settle down to a steady state with a fixed separation [78]. For the NRCH model, we find that the defect interactions depend on their relative topological charge, the non-reciprocity coupling parameter α, and the initial inter-defect separation Λ (see figure 1 for typical configurations of defects). The primary factor that leads to a novel phenomenological behaviour is the stability of the topologically neutral targets. When placed at a separation smaller than a threshold Λ_{SS}, oppositely charged spirals annihilate to create targets (see figure 8 and Movie 2). At low α, a pair of like-charged spirals form bound pairs where the spirals orbit around a common centre, whereas for larger values of α, we observe spontaneous creations of targets in between the pair (see Movie 2). A spiral-target pair evolves into a single spiral at low values of α. With increasing α, we find that the behaviour of the system depends on the initial separation as well. The final state below a threshold Λ_{ST} is a spiral, whereas above Λ_{ST} it is a target (see figure 8). A pair of targets behaves in a similar manner to a pair of oppositely-charged spirals, but with a different threshold separation Λ_{TT} (see figure 8).

In section 2, we introduce our model and provide a brief summary of the properties of isolated defect solutions, previously reported in [14]. In section 3, we describe the properties of the quasi-stationary defect networks. To explain the features of defect networks, we study interactions between two defects with different relative charges in section 4. We conclude the paper with a discussion and possible future directions in section 5.

2. Model and methods

2.1. The NRCH model

We consider a two species NRCH model of phase separating mixtures [3–5, 14, 81] with non-reciprocal interactions. The conserved dynamics of the two scalar fields $\phi_1(\boldsymbol{r},t)$ and $\phi_2(\boldsymbol{r},t)$ is described by the continuity equation $\partial_t\phi_a = -\boldsymbol{\nabla}\cdot\boldsymbol{\mathcal{J}}_a$, where $\boldsymbol{\mathcal{J}}_a$ is the current for the ath species, with $a = 1,2$. In equilibrium, the density currents are obtained from the gradient of the equilibrium chemical potentials $\mu_a = \delta\mathcal{F}/\delta\phi_a$, where $\mathcal{F}$ is the free energy. We introduce a complex scalar order parameter $\phi = \phi_1 + i\phi_2$ and choose the following form of the free energy

$$\mathcal{F} \equiv \int \mathrm{d}\boldsymbol{r}\left(-\frac{1}{2}|\phi|^2 + \frac{1}{4}|\phi|^4 + \frac{1}{2}|\boldsymbol{\nabla}\phi|^2\right), \tag{1}$$

which describes phase separation with reciprocal interactions and is invariant under the rotations in ϕ-space. The equilibrium dynamics can be written as

$$\partial_t\phi = -\boldsymbol{\nabla}\cdot\boldsymbol{\mathcal{J}}; \quad \boldsymbol{\mathcal{J}} \equiv -\boldsymbol{\nabla}\left(\frac{\delta\mathcal{F}}{\delta\phi^*}\right), \tag{2}$$

where $\boldsymbol{\mathcal{J}} = \boldsymbol{\mathcal{J}}_1 + i\boldsymbol{\mathcal{J}}_2$ and ϕ^* is the complex conjugate of ϕ. We now introduce an additional density current $-\boldsymbol{\nabla}(i\alpha\phi)$ (or an additional non-equilibrium imaginary contribution of $i\alpha\phi$ to the chemical potential), which arises from non-reciprocal interactions between the 1 and 2 species [3], namely, a chasing interaction in which 1 is attracted to 2 with strength α (for $\alpha > 0$) when 2 is repelled by 1 by the same strength [1, 2]. As it is not possible to derive this current from a free energy functional, it can be expected that it can drive the system out of equilibrium. Thus, α measures the degree of the non-reciprocity in the system. The non-equilibrium dynamics can then be written as

$$\partial_t\phi = -\boldsymbol{\nabla}\cdot[\boldsymbol{\mathcal{J}} - i\alpha\boldsymbol{\nabla}\phi]. \tag{3}$$

Substituting the values of different expressions, we obtain the NRCH model

$$\partial_t\phi = \boldsymbol{\nabla}^2\left[(-1+i\alpha)\,\phi + |\phi|^2\phi - \boldsymbol{\nabla}^2\phi\right], \tag{4}$$

which describes out of equilibrium phase separation for two species with non-reciprocal interactions.

2.2. Relevant time and length scales

The length and time scales of interest are as follows:

- The spinodal instability cutoff length ℓ and the spinodal time scale τ, which govern the evolution of small perturbations to the homogeneous state $\phi = 0$, are set to unity in the above equation. In other words we measure distances in units of ℓ and time in units of τ.
- The non-reciprocal length and time scales are $\ell_\alpha = \ell/\sqrt{\alpha}$ and $\tau_\alpha = \tau/\alpha^2$. They govern the oscillatory features of the dynamics of the system.
- The system size is denoted as L and the total evolution time is called T. To be able to probe the long-time and large-scale dynamics, we require $L \gg \ell_\alpha$ and $T \gg \tau_\alpha$. As shown in [14], small system sizes can lead to finite size effects and alter the phenomenology.

We note here that we have chosen to work with a non-dimensional version of the NRCH model which was previously studied in [14]. For a detailed description and phenomenological derivation of the NRCH model we refer the reader to [3–5, 14, 81].

2.3. Isolated defect solutions

The NRCH model (4) admits a variety of novel non-equilibrium states as has been shown recently [3–5, 15, 16]. Here, we study the properties of the defect networks emerging from the time evolution of an initial disordered state as we have reported recently in Rana and Golestanian [14]. We start with a discussion on the properties of an isolated defect solution, which is of the form

$$\phi(\boldsymbol{r}, t) = R(r)\, e^{i[m\theta + Z(r) - \omega t]}, \tag{5}$$

where r (as measured from the defect core) and θ are the polar coordinates, $R(r)$ is the amplitude, $Z(r)$ is the phase, and m is the topological charge. An isolated spiral core ($m = \pm 1$) is singular and stationary, thus $R(r)$ vanishes at the origin and is independent of time. On the other hand, a target ($m = 0$) is topologically neutral and its amplitude remains finite at the core while oscillating slowly [14, 79, 82, 83].

Irrespective of the value of m, defects emanate radially outward travelling waves, and far away from the defect core ($r \gg 1$) the wave front approaches a plane wave, i.e. $k(r) \equiv \mathrm{d}Z(r)/\mathrm{d}r \to k_\infty$, $R(r) \to R_\infty = \sqrt{1 - k_\infty^2}$. For smooth matching of the oscillatory behaviour at all distances from the defect, we need to choose the frequency as $\omega = \alpha k_\infty^2$ [14]. The equivalence of the charged and neutral defects in the context of the generated travelling waves becomes clear by looking at the polar order parameter

$$\boldsymbol{J}(\boldsymbol{r}, t) \equiv \frac{1}{2i}\left(\phi^* \boldsymbol{\nabla}\phi - \phi \boldsymbol{\nabla}\phi^*\right). \tag{6}$$

For monochromatic travelling waves, $\boldsymbol{J}$ is parallel to the wave vector of the wave. On the other hand, $\boldsymbol{J} = R(r)^2\left(k(r)\hat{\boldsymbol{r}} + \frac{m}{r}\hat{\boldsymbol{\theta}}\right)$ for the spirals and targets. Independently of the value of m, $\boldsymbol{J}$ has a unit positive topological singularity at the defect core. Far away from the core, $\boldsymbol{J} \sim R_\infty^2 k_\infty \hat{\boldsymbol{r}}$ is purely radial. Since $\boldsymbol{J}$ is isotropic, the average polar order $\bar{J} \equiv \left|\left\langle \widehat{\boldsymbol{J}}(\boldsymbol{r}, t)\right\rangle\right| = 0$ for isolated defects. Consequently, disordered defect networks have vanishing average polar order.

2.4. Numerical methods

We use a GPU-accelerated pseudo-spectral algorithm to numerically integrate the equation of motion (4) on a two-dimensional periodic box with sides (L_x, L_y) discretized over (N_x, N_y) points. For time marching, we use a second-order exponential time-differencing scheme [84]. For simulations that start from random initial conditions, we use the same setup as used in [14] and set $L_x = L_y = L$ and $N_x = N_y = N$ with $L = 6400$ and $N = 4096$. We evolve the system up to $T = 4 \times 10^5$ and choose the time step $\Delta t = 2 \times 10^{-1}$. Throughout the time evolution, we monitor various measures that characterize the system, for example the position and number of the defect cores, as well as the polar order parameter. The setup for the defect interaction simulations follows Aranson *et al* [78] and is described in section 4.

2.5. Finding the defect cores

To identify the spiral and target cores, we use a topological charge counting algorithm [85] adopted for two dimensions. While the algorithm locates the spirals cores in a straightforward manner, it cannot find the location of the topologically neutral targets. In addition, the algorithm also gives the undesirable topological zeroes present at the intersection of the disinclination lines (see figure 4(b), for example). Both of these issues

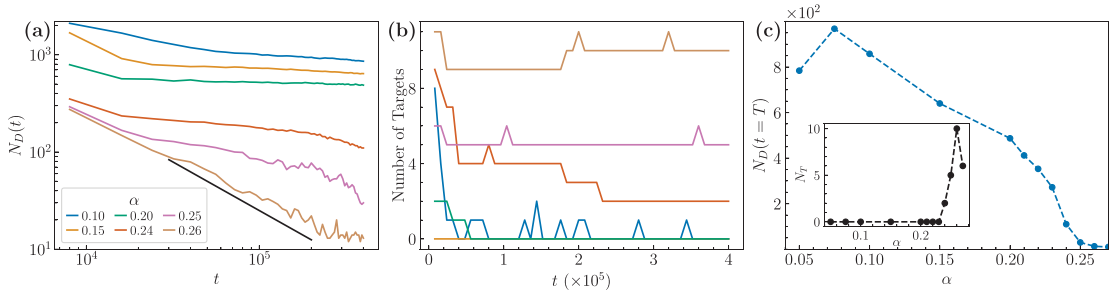

Figure 2. (a) Evolution of the number of defects with time. At later times, the number of defects decays slowly. For small α, we find $N_D(t) \sim 1/t^{0.1}$. For $\alpha = 0.26 \sim \alpha_c$, we observe $N_D(t) \sim 1/t$. (b) The number of targets with time. For $\alpha > 0.2$, we find a constant number of targets versus time. (c) The number of defects at the end of the simulation ($t = T$). Inset: the number of targets. For a detailed discussion on the number density, see [14].

are easily resolved by exploiting the properties of the polar order parameter $\boldsymbol{J}(\boldsymbol{r}, t)$ (6). To find the defect cores of ϕ, we first find the topological zeros of the polar current $\boldsymbol{J}$ carrying a positive unit charge. We then calculate the topological charge of ϕ to classify them into spirals and targets. To eliminate the defects on the disinclination lines, we introduce the quantity $Q = \frac{1}{A_\Omega}\int_\Omega \boldsymbol{J}\cdot\boldsymbol{\Delta r}\mathrm{d}\Omega$, where $\boldsymbol{\Delta r}$ is measured from the defect core, and Ω is a small domain around the defect with area A_Ω. As $\boldsymbol{J} \sim \hat{r}$, Q is large and positive for isolated spirals and targets. On the other hand, $\boldsymbol{J}$ changes with orientation for the defects on the disinclination lines and the absolute value of Q is small. A suitable threshold of Q, which we choose heuristically, then filters out the defects on the disinclination lines.

3. Disordered defect networks

For non-reciprocity coupling smaller than the critical threshold α_c, an initially disordered configuration evolves into a quasi-stationary defect network. The defect network emerges after an initial transient period in which numerous newly-born defects move around and merge to form a very slowly evolving configuration [14]. In figure 1, we plot the location of the defects in the defect networks for various values of α. The defect networks are composed of isolated spiral and target cores separated from each other by distances larger than the core radius. At low values of α, we observe isolated spirals and bound pairs of like-charged spirals that revolve around a common centre. As we increase α, targets emerge and dominate the system for α just below α_c.

3.1. Number of defects

In figure 2(a) we plot the time evolution of the number of defects $N_D(t)$. We observe a quick decrease in the beginning ($t \lesssim 2 \times 10^4$), followed by a substantially slower regime, where $N_D(t)$ decreases as a power law. For α as high as 0.20, this decay can be extremely slow (we find $N_D(t) \sim t^{-0.1}$ for $\alpha = 0.1$ and $N_D(t) \sim t^{-0.04}$ for $\alpha = 0.2$ using least square fits) and the defect networks are effectively arrested in time. For α close to α_c, we find $N_D(t) \sim 1/t$. In figure 2(b), we plot the evolution of the number of targets for different α. For $\alpha < 0.2$, the number of targets rapidly goes to zero, while for $\alpha > 0.2$, we find a steady number of targets. Occasionally, we observe some target creation events, which are recorded as blips in the lines. As will be discussed later, the merger of oppositely-charged spirals and spontaneous creation of targets at large α leads to these events. In figure 2, we plot the number of defects at the final state for $L = 6400$, which shows that the average number of defects decreases with increasing α. For $\alpha \gtrsim 0.25$ there are only a handful of defects in the system as is also evident from figure 1, most of which are targets (see also figure 2((c), inset)). A comprehensive data set describing the evolution of the defect density, comparing different box sizes and multiple realizations of the initial conditions has already been reported in [14]. As was shown in [14], the precise spatial distribution of the defects depends highly on the initial conditions. Consequently the defect density can vary across different realizations of the initial disordered state. However, for $\alpha < \alpha_c$, our tests show that a randomly chosen defect configuration respecting the typical inter-defect separation and defect density always forms a stable defect network.

3.2. Inter-defect separation

We now describe the spatial organization of the defect networks. From the snapshots figure 1, we find that the average nearest-neighbour separation appears to increase with α, while the targets show a strikingly higher inter-defect separation as compared to the spirals. An observable of interest that characterizes the

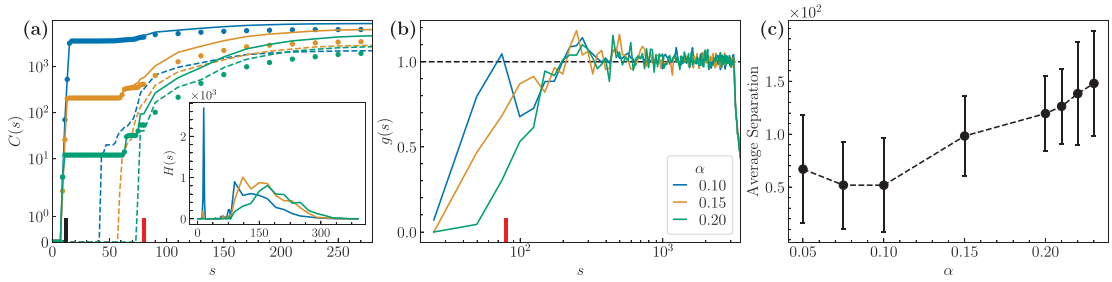

Figure 3. (a) Cumulative histogram of the nearest-neighbour separation $C(s)$ for different values of α. $C(s)$ rises sharply in the beginning and then stays constant for intermediate distances, followed by a subsequent rise in steps. An accompanying decrease in the number of defects contributes to the initial rise in $C(s)$. Inset: the histogram of $H(s)$. (b) Radial distribution function $g(s)$ versus s. For $s > 100$, $g(s)$ is constant, implying that the defects are uniformly distributed on the domain. (c) Average inter-defect separation as a function of α. In (a) and (b), we also mark the approximate position of s_{peak} and s_{broad} on the $x-$axis with black and red lines, respectively.

defect distribution is the nearest-neighbour separation s. We compute the histogram $H(s)$, as well as its cumulative sum $C(s)$, and plot them in figure 3(a) for different values of α. $C(s)$ is negligible up to $s_{\text{peak}} \sim 10$ and then rises sharply, implying the presence of a significant number of defects with a nearest-neighbour separation s_{peak}. The number of defects that contribute to this rise is large at small α, and it decreases with increasing α. There are almost no defects with an intermediate nearest-neighbour separation, as can be seen by a plateau in $C(s)$ for $s_{\text{peak}} < s < s_{\text{broad}} \sim 80$. Above s_{broad}, $C(s)$ increases slowly, implying a broad distribution at large values of s. These features are also evident in the plot of $H(s)$ as shown in figure 3((a), inset). We further filter the statistics of the nearest-neighbour separation on the basis of the relative topological charge between the neighbours and find that only the like-charged spirals contribute to the rise at small s. $C(s)$ for nearest neighbours with the same topological charge matches exactly with the unfiltered $C(s)$ for $s < s_{\text{broad}}$. On the other hand, $C(s)$ for nearest neighbours with opposite topological charges stays zero for $s < s_{\text{broad}}$ and contributes only to the broad distribution for $s > s_{\text{broad}}$. It means that there are no nearest neighbours with opposite topological charges at separations below s_{broad}. In section 4, we will show that these features of $C(s)$ and $H(s)$ are essentially related to the interactions between a pair of like- or oppositely-charged spirals. In figure 3(b) we plot the radial distribution function for the defects and find that $g(s)$ is more or less constant, implying that the defects are uniformly distributed in space. Figure 3(c) shows the variation of average nearest-neighbour separation, which first decreases, and then appears to increase with α, while showing large variability due to the broad distribution of the nearest-neighbour separation.

3.3. Moving defects and disinclination lines

In the slow phase where the number density evolves slowly, defect networks can be considered effectively arrested in time. In this phase, most of the dynamics of isolated spiral and target cores is limited to emanating travelling waves. While doing so, the arms of the isolated spirals rotate with the frequency ω and the targets pulsate. The like-charged spirals form a bound pair and orbit around a common centre (this phenomenon will be discussed in detail in section 4). Occasionally we find a spiral moving in a circular arc (see figure 4(a)) while its neighbours remain stationary. A visual inspection of the spiral and its neighbours reveals that they all carry the same topological charge. The motion then possibly emerges from unbalanced interactions among like-charged spirals.

Disinclination lines are formed where the waves generated by two or more defects meet. The shape of the disinclination lines is easily determined by phase matching of the nearby spiral/target cores [79, 86]. As shown in figure 4, they are well approximated as segments of hyperbole whose foci are the two nearest defects, i.e. $r_1 - r_2 = c$, where c is a constant and r_1 and r_2 are the distances from the two nearest defects (with $r_1 < r_2$). Additional topological defects emerging from zeros of the ϕ-field are found where multiple disinclination lines meet. These defects are separated from each other by distances comparable to the core radius ℓ. They undergo periodic dynamical rearrangements without affecting the spiral and target dynamics, as they are unable to settle down into a stable stationary state [14].

4. Defect interactions

The quasi-stationary nature of the defect networks hints that the interactions between defects may fall rapidly with increasing separation. Similar behaviour is observed for the CGL equation, where the defect

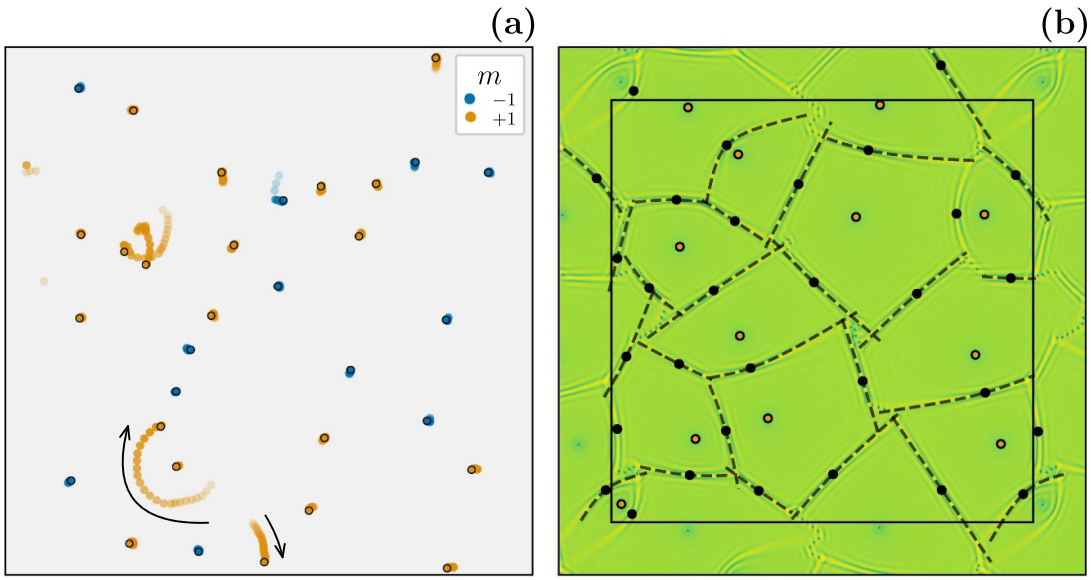

Figure 4. (a) Motion of spiral cores in a disordered defect network. Time is marked by increasing opacity of the markers and the direction of motion is highlighted for two spirals using black arrows. The final position of each defect is marked by a black hollow marker. A few spiral cores are easily seen to orbit around like charged neighbours. (b) Hyperbole construction [86] for a particular realization of a defect network for $\alpha = 0.18$. We extend the periodic domain (shown by solid black square) on all four sides to generate the construction. Constructed hyperbole segments are shown by dashed black lines. Orange circles mark the location of the defect cores that are the foci of the hyperbole (all spirals for this particular α), whereas black circles mark the points on the disinclination lines that were used to measure the distance from the foci.

interactions decay exponentially [77, 78, 80]. Thus we expect that the nearest neighbour interactions are enough to determine the properties of the defect networks. To this end, we numerically study the interactions of a defect-pair with different relative topological charges separated by a varying initial distance Λ. For these simulations, we consider a rectangular box with sides $(L_x, L_y) = (L, 2L)$ divided into four equal quadrants of size $(L/2, L)$ to approximate no-flux boundary conditions in a periodic domain. Unless specified otherwise, we set $L = 200$ and discretize the domain with $(512, 1024)$ grid points. Typically, the time it takes for a defect pair to evolve into a different configuration is of the order of tens of τ_α. For the smallest α considered here, this time scale is of the order of $\sim 4 \times 10^2$. We evolve each defect configuration for at least up to $T = 4 \times 10^3$ with a time step $\Delta t = 4 \times 10^{-2}$. For oppositely charged spirals, target-target pair, or a spiral-target pair, it is enough to reach a state where either they have merged or remain stable as a pair. For like-charged spirals at larger separations we evolve as long as $T = 2 \times 10^5$ such that they complete at least one full revolution in the orbit.

Initially, a defect is placed in the lower left quadrant at coordinates $\left(\frac{L}{2} - \frac{\Lambda}{2}, L\right)$. The field is then extended to the upper left quadrant by symmetric reflection along the line $y = L$ resulting in a pair of oppositely charged spirals in the left half of the domain. A further symmetric (anti-symmetric) reflection along $x = L/2$ line gives us a pair of oppositely (like) charged spirals separated by a distance Λ apart (see figure 5). Unlike the study of Aranson *et al* [78], we perform this symmetrization only at the beginning of the simulation. Since the targets do not break the mirror symmetry, the same procedure is also used to generate target pairs. This procedure leads to two pairs of defects, or a total four defects in the rectangular domain. As $\Lambda < L$, the dominant interactions are among the horizontal neighbours and the two pairs evolve independently to each other in an identical manner. Thus, in the following discussion, we focus on the dynamics of one pair only. Finally, we note here that we have performed a systematic numerical study of the defect interactions for $\alpha \leqslant 0.35 < \alpha_\times$. As we move closer to $\alpha_\times \sim 0.58$, numerical perturbations and finite-size effects tend to destabilize the initial defect-pair configurations or the final steady-states.

In the rest of this paper, we will show that defects in the NRCH model show new kind of interactions, largely facilitated by the stability of the topologically neutral targets. As summarized in figure 6, the evolution of the pair depends on the relative topological charges on the defects, the initial separation Λ, and the strength of the non-reciprocal interactions α. As expected, at large initial separation Λ, irrespective of the relative topological charges, interactions are small and the defect pair remains stationary or evolve at slow time scales. For example, like-charged spirals in larger orbits revolve with velocities that are an order of

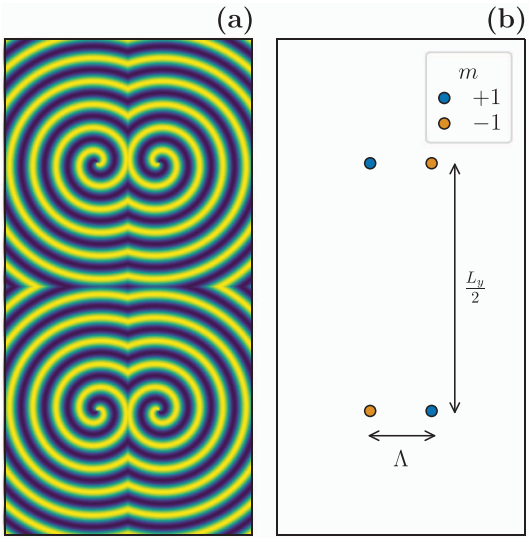

Figure 5. Simulation setup used to study interactions among defect pairs. (a) Initial condition for like-charged spirals and (b) schematic diagram. There are two defect pairs, one in the lower half of the domain and the other in the upper half of the domain. Defect pairs are far apart from each other ($\frac{L_y}{2} > 2\Lambda$), and thus are expected to have negligible interactions between them. Because of the reflection symmetry with respect to the $y = \frac{L_y}{2}$ line, the spirals in upper pair have the opposite charge as compared to the spirals in the lower pair.

Defect Pair	Low α		High α	
	Small Λ	Large Λ	Small Λ	Large Λ
Targets	Singlet	Pair	Singlet	Pair
Spiral-Target	Singlet	Singlet	Singlet	Singlet
Like Spirals	Orbiting Pair	Orbiting Pair	Singlet	Singlet
Opposite Spirals	Singlet	Pair	Singlet	Pair

Figure 6. A qualitative summary of pairwise defect interactions for different initial configuration, initial separation Λ, and non-reciprocity coupling α. For each case, we list the final state. Final state listed as 'Singlet' means that the initial configuration of two defects evolved into a single defect. 'Pair' means that the two initial defects do not evolve into another configuration. The colour marks the topological charge of the final state: green means target and purple means spiral. For example, at low α and small Λ, a spiral-target configuration evolves into a single spiral marked by 'Singlet' on the purple background. See figure 8 for a discussion on the evolution of Spiral-Target, Target-Target and Oppositely-charged Spiral configurations. See figure 7 for a discussion on the evolution of like charged spirals.

magnitude smaller as compared to the smaller orbits (see figure 7). On the full time scale of the simulations, oppositely-charged spirals at large separations travel small distances as compared to the system size. In what follows, we describe our results for small and intermediate separations for different α values, and use them to explain the properties of the defect networks.

4.1. Like-charged spirals

The evolution of a like-charged spiral pair shows rich behaviour which can be broadly separated into two distinct regimes depending upon the strength of the non-reciprocity coupling α.

Small α—As shown in figures 7(a) and (b), for small $\alpha \lesssim 0.3$, two like-charged spirals settle in an orbit and revolve around a common centre (see Movie 1). These orbiting like-charged spirals can be thought of as a bound-pair or a single spiral with topological charge $m = 2$. Depending on the initial separation, the pair settles into one of the possible orbits (see figure 7(a)). In these orbits, the separation between two spirals varies sinusoidally with time, although the total variation is small compared to its average value (i.e. $<10\%$, see figure 7(b)). The average separation Λ_O and the angular velocity V_O depend on α. We find that Λ_O decreases with α as $\Lambda_O \sim 1/\sqrt{\alpha}$. In the smallest orbit, V_O increases as $\alpha^{3/2}$ (see figure 7(d)), while for the larger orbits, the data deviates significantly from the power-law form. In figure 7(d), we also compare Λ_O in the smallest orbit with s_{peak}, the distance at which $H(s)$ shows a sharp peak. We find that the two are in

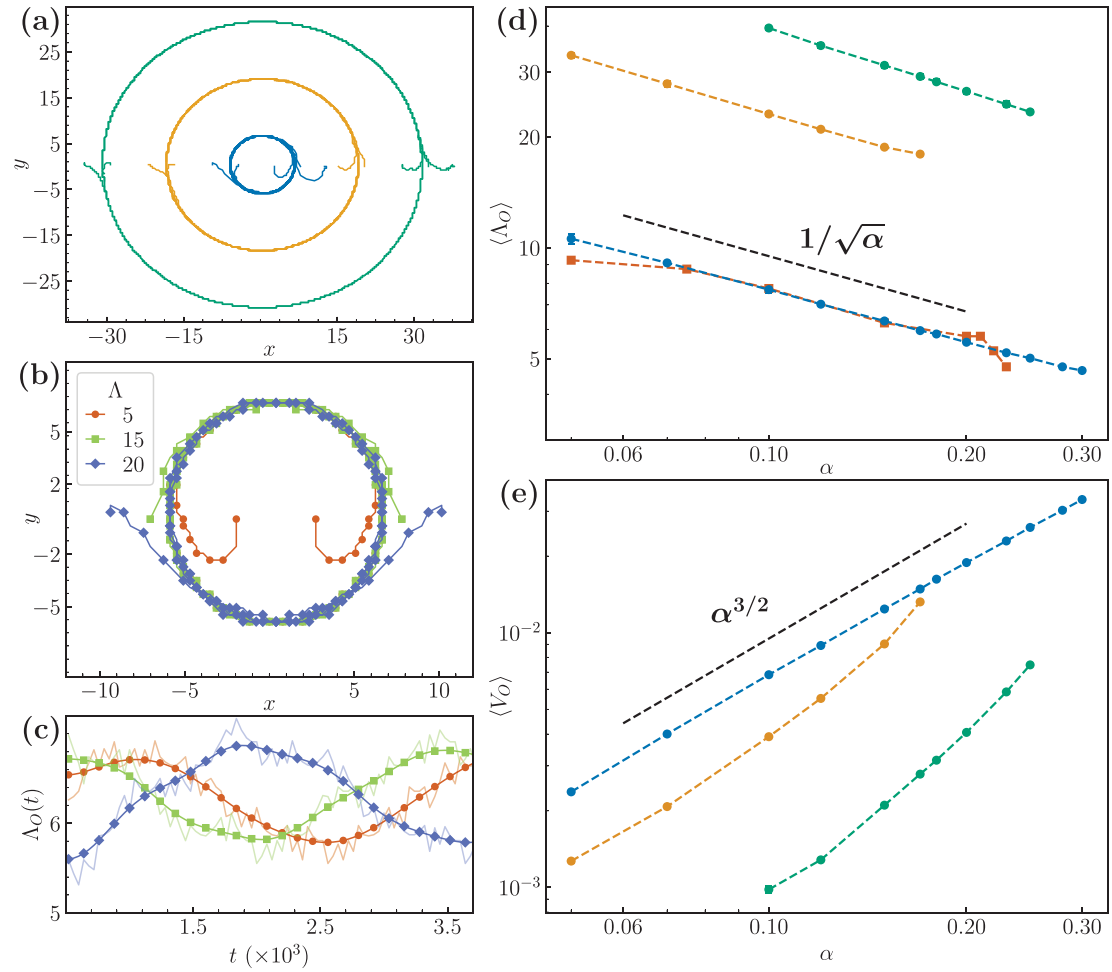

Figure 7. (a) Evolution of two like-charged spirals for $\alpha = 0.15$. The spirals settles into well-defined orbits where they revolve around a common centre, with the size of the orbit depending on the initial separation. (b) Zoomed-in view of the innermost orbit for three different initial separations, showing that irrespective of the initial separation the orbit size stays the same. (c) In the orbits, inter-spiral separation varies sinusoidally with time. Light lines show the actual orbit over time, and the markers show the smoothed data. (b) and (*c*) share the same legend. (d) and (e) Plot of average separation in the orbit $\langle\Lambda_O\rangle$ and the average angular velocity $\langle V_O\rangle$ versus α for different orbits. In both the plots, different colours represent orbits of different size, as shown in (a). Error bars indicate root mean-square deviation from the mean, and are of the same size as the markers. We find $\langle\Lambda_O\rangle \sim 1/\sqrt{\alpha}$ for all the orbits and $\langle V_O\rangle \sim \alpha^{3/2}$ for the smallest orbit, consistent with $\langle\Lambda_O\rangle/\tau_\alpha$. For larger orbits, $\langle V_O\rangle$ deviates significantly from a power law form. In (d), we also plot s_{peak} (red markers with solid line), which matches very well with the $\langle\Lambda_O\rangle$ for the smallest orbit, verifying that the interaction between the like-charged spirals contributes to the sharp rise in $C(s)$ at s_{peak}.

excellent agreement, implying that the interactions between the like-charged spirals determine the properties of the defect networks at the smallest scales. As discussed earlier, we find pairs of like-charged spirals orbiting around each other in our simulations starting from random initial states (see Movie 2 in [14]) as well as a spiral rotating around a like-charged neighbour which remains stationary (see figure 4(a)).

Large α—For $\alpha \gtrsim 0.3$, the spirals initially form a bound pair and start to rotate around each other. At later times, however, a target forms spontaneously on the line joining the spiral cores and pushes the spirals outwards (see Movie 1). Since periodicity ensures that the net charge over the entire domain is zero, we thus obtain a target defect at the centre of the domain at long times.

4.2. Oppositely-charged spirals

When placed closer than a threshold separation Λ_{SS}, a pair of oppositely-charged spirals annihilate to form a single target. This scenario is allowed because targets are stable solutions of the NRCH model (4), but it has no counterpart in the CGL equation. It also explains the fact that there are no oppositely-charged neighbours at small separations in the defect networks. As shown in figure 8(a), the threshold separation varies in a non-trivial manner with α. At certain values of α, sharp rises are observed in Λ_{SS}, accompanying otherwise slow variations. When placed at distances larger than the threshold value Λ_{SS}, the spiral pair is stable and moves in a direction perpendicular to the line joining their centres. Similar to the oppositely-charged spirals

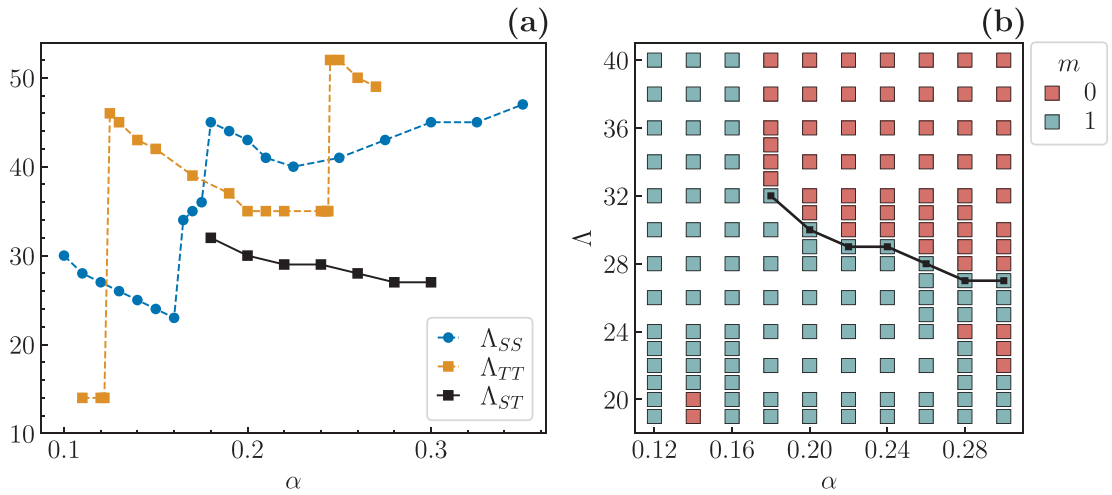

Figure 8. (a) The threshold separations Λ_{SS}, Λ_{ST}, and Λ_{TT} for various values of α. Λ_{SS} and Λ_{TT} reported here are for $L_y = 2L_x = 600$, which are also consistent with $L_y = 400$. For $\Lambda < \Lambda_{SS}$, two oppositely-charged spirals merge to form a target, while for $\Lambda > \Lambda_{SS}$, the pair is stable. For $\Lambda < \Lambda_{TT}$, two targets merge. (b) Phase plot showing final state of a spiral-target pair at various values of α and initial separation Λ. At low α, the pair almost always evolves into a single spiral. For $\alpha \geqslant 18$, the evolution depends on Λ_{ST}. For $\Lambda < \Lambda_{ST}$, a spiral target pair evolves into a single spiral, while beyond Λ_{ST}, it evolves into a target.

in the CGL equation [78], the tangential velocities for the two spirals are parallel, and decrease as the initial separation increases. For $\Lambda \gg \Lambda_{SS}$ or for small α, the velocity at which the pair moves is small. For example, for $\alpha = 0.2$ and $\Lambda = 50$, the spirals move a distance of $\sim 0.04 L_y$ over the entire simulation duration.

4.3. A target pair

A pair of targets shows similar features as a pair of oppositely-charged spirals. Below a threshold initial separation Λ_{TT}, the pair merges to form a single target. Above Λ_{TT}, the pair is stable (see Movie 3). However, as they are topologically neutral, the stable target pair remains stationary. As shown in figure 8, Λ_{TT} varies in a manner similar to Λ_{SS}. It shows sharp rises at $\alpha = 0.12$ and $\alpha = 0.24$, and decreases slowly otherwise.

4.4. A spiral and a target

We summarize the fate of a spiral-target configuration in the $\alpha - \Lambda$ state diagram shown in figure 8(b). For $\alpha < 0.18$, irrespective of the initial separation, a spiral-target pair eventually merges to form a single spiral. For $\alpha \geqslant 0.18$, a threshold of initial separation Λ_{ST} marks the change in the final state. For $\Lambda < \Lambda_{ST}$, the pair evolves into a single spiral. Above Λ_{ST}, the outward travelling waves emitted from the target tear the spiral core apart pushing it radially outwards. Owing to the periodic boundary conditions, we are left with a single target. As shown in figure 8, Λ_{ST} decreases with α. We note that there are a few exceptions to this overall consistent behaviour, particularly at small values of Λ.

5. Discussion

We have presented here a detailed numerical analysis of the properties of the defect networks as well as the interaction of the defects in the NRCH model. While both charged and neutral solutions are allowed for a given α, our study reveals an intriguing selection mechanism that favours either spirals or targets. At small α, the system prefers to spontaneously break chiral symmetry and select spirals. On the other hand, at large values of α, targets are the dominant defects. The defect solutions of the NRCH model share some features with those of the CGL equation, for example wavenumber selection and the ability to form extremely slowly evolving defect networks, while exhibiting novel types of interactions. This is facilitated mainly by the stability of the topologically neutral target solutions. Importantly, we find that the defect interactions depend on the relative topological charges as well as the strength of non-reciprocity. This is in a direct contrast to the defect interactions for the CGL equation, where irrespective of the topological charge, spirals repel each other. Furthermore, we show that the time evolution of defect pairs readily explains the dynamics of the observed defect networks. The interactions between a pair of like-charged spirals and their ability to form bound states where they orbit around a common centre determine the nearest-neighbour configuration at the smallest scales. The selection mechanism is also explained by the interaction between a spiral and target,

which exclusively evolves the system into spirals for small α, but can result in either a spiral or a target at large α depending upon the initial separation.

While we have performed large-scale and long-time simulations, we find that the defect networks evolve very slowly with time. For example, for $\alpha < \alpha_c$, we find that the defect density decays as a power law with an exponent as small as 0.1. Thus, defect networks are extremely long-lived states. For the CGL equation, defect networks show similar behaviour and are known to show a vortex liquid phase where spirals exhibit normal diffusion or a vortex glass state with intermittent slow relaxation [87]. It will be interesting to see the behaviour of the defect networks for the NRCH model on even longer time scales.

Data availability statement

All data that support the findings of this study are included within the article (and any supplementary files).

Appendix. Description of the movies

- **`movie1_like_charged.mkv`** shows the evolution of a like-charged spiral pair configuration for $\alpha = 0.2$ and 0.35. At $\alpha = 0.2$, the spirals form a bound pair and orbit around a common point with constant angular velocity (see figure 7). At $\alpha = 0.35$, a target emerges spontaneously at the centre of the line joining the spiral pair and pushes the spirals away. Since the net charge on the periodic domain is zero, the final state is a target.
- **`movie2_opposite_charged.mkv`** shows the evolution of an oppositely charged pair of spirals for $\Lambda = 30$ and 50 at $\alpha = 0.2$. For $\Lambda = 30 < \Lambda_{SS}$, the spirals merge and form a single target (see figure 8(a)). For $\Lambda = 50 > \Lambda_{SS}$ the pair remains stable and move in a direction perpendicular to the line joining their centres.
- **`movie3_targets.mkv`** shows the time evolution of a target pair for $\Lambda = 25$ and 50 at $\alpha = 0.2$. The dynamics of the target pair is similar to a pair of oppositely charged spirals. For $\Lambda = 25$, the target pair merge and form a single target. For $\Lambda = 50$ the pair remains stable and stationary.
- **`movie4_spiral_and_target.mkv`** shows the time evolution of a spiral-and-target pair for $\Lambda = 25$ and 40 at $\alpha = 0.2$, where a threshold separation Λ_{ST} marks the change in behaviour. For $\Lambda = 25 < \Lambda_{ST}$, the pair merges to form a single spiral, whereas for $\Lambda = 40 > \Lambda_{ST}$ the pair merges to form a single target (see figure 8).

ORCID iDs

Navdeep Rana https://orcid.org/0000-0002-4432-3982
Ramin Golestanian https://orcid.org/0000-0002-3149-4002

References

[1] Soto R and Golestanian R 2014 Self-assembly of catalytically active colloidal molecules: tailoring activity through surface chemistry *Phys. Rev. Lett.* **112** 068301
[2] Agudo-Canalejo J and Golestanian R 2019 Active phase separation in mixtures of chemically interacting particles *Phys. Rev. Lett.* **123** 018101
[3] Saha S, Agudo-Canalejo J and Golestanian R 2020 Scalar active mixtures: the nonreciprocal Cahn-Hilliard model *Phys. Rev.* X **10** 041009
[4] You Z, Baskaran A and Marchetti M C 2020 Nonreciprocity as a generic route to traveling states *Proc. Natl Acad. Sci.* **117** 19767–72
[5] Saha S and Golestanian R 2022 Effervescent waves in a binary mixture with non-reciprocal couplings (arXiv:2208.14985)
[6] Fruchart M, Hanai R, Littlewood P B and Vitelli V 2021 Non-reciprocal phase transitions *Nature* **592** 363–9
[7] Ballerini M *et al* 2008 Interaction ruling animal collective behavior depends on topological rather than metric distance: evidence from a field study *Proc. Natl Acad. Sci.* **105** 1232–7
[8] Helbing D and Molnár P 1995 Social force model for pedestrian dynamics *Phys. Rev.* E **51** 4282–6
[9] Helbing D, Farkas I and Vicsek T 2000 Simulating dynamical features of escape panic *Nature* **407** 487–90
[10] Rio K W, Dachner G C and Warren W H 2018 Local interactions underlying collective motion in human crowds *Proc. R. Soc.* B **285** 20180611
[11] Osat S and Golestanian R 2023 Non-reciprocal multifarious self-organization *Nat. Nanotechnol.* **18** 79–85
[12] Ivlev A V, Bartnick J, Heinen M, Du C-R, Nosenko V and Löwen H 2015 Statistical mechanics where Newton's third law is broken *Phys. Rev.* X **5** 011035
[13] Dadhichi L P, Kethapelli J, Chajwa R, Ramaswamy S and Maitra A 2020 Nonmutual torques and the unimportance of motility for long-range order in two-dimensional flocks *Phys. Rev.* E **101** 052601
[14] Rana N and Golestanian R 2024 Defect solutions of the nonreciprocal Cahn-Hilliard model: spirals and targets *Phys. Rev. Lett.* **133** 078301
[15] Frohoff-Hülsmann T, Wrembel J and Thiele U 2021 Suppression of coarsening and emergence of oscillatory behavior in a Cahn-Hilliard model with nonvariational coupling *Phys. Rev.* E **103** 042602
[16] Frohoff-Hülsmann T and Thiele U 2021 Localized states in coupled Cahn–Hilliard equations *IMA J. Appl. Math.* **86** 924–43
[17] Frohoff-Hülsmann T and Thiele U 2023 Nonreciprocal Cahn-Hilliard model emerges as a universal amplitude equation *Phys. Rev. Lett.* **131** 107201

[18] Golestanian R 2022 Phoretic active matter *Active Matter and Nonequilibrium Statistical Physics: Lecture Notes of the Les Houches Summer School: Volume 112, September 2018* (Oxford University Press) (https://doi.org/10.1093/oso/9780192858313.003.0008)
[19] Tucci G, Golestanian R and Saha S 2024 Nonreciprocal collective dynamics in a mixture of phoretic Janus colloids *New J. Phys.* **26** 073006
[20] Nelson D R 2002 *Defects and Geometry in Condensed Matter Physics* (Cambridge University Press)
[21] Chaikin P M and Lubensky T C 1995 *Principles of Condensed Matter Physics* (Cambridge University Press)
[22] Chandrasekhar S 1992 *Liquid Crystals* 2nd edn (Cambridge University Press)
[23] Romano J, Mahault B and Golestanian R 2023 Dynamical theory of topological defects I: the multivalued solution of the diffusion equation *J. Stat. Mech.* 083211
[24] Romano J, Mahault B and Golestanian R 2024 Dynamical theory of topological defects II: universal aspects of defect motion *J. Stat. Mech.* 033208
[25] Hadzibabic Z, Krüger P, Cheneau M, Battelier B and Dalibard J 2006 Berezinskii–Kosterlitz–Thouless crossover in a trapped atomic gas *Nature* **441** 1118–21
[26] Hindmarsh M B and Kibble T W B 1995 Cosmic strings *Rep. Prog. Phys.* **58** 477
[27] Kosterlitz J M and Thouless D J 1973 Ordering, metastability and phase transitions in two-dimensional systems *J. Phys. C: Solid State Phys.* **6** 1181–203
[28] Shankar S, Ramaswamy S, Marchetti M C and Bowick M J 2018 Defect unbinding in active nematics *Phys. Rev. Lett.* **121** 108002
[29] Bray A J 2002 Theory of phase-ordering kinetics *Adv. Phys.* **51** 481–587
[30] Abrikosov A A 2004 Nobel lecture: type-II superconductors and the vortex lattice *Rev. Mod. Phys.* **76** 975–9
[31] Yurke B, Pargellis A N, Kovacs T and Huse D A 1993 Coarsening dynamics of the *XY* model *Phys. Rev.* E **47** 1525–30
[32] Qian H and Mazenko G F 2003 Vortex dynamics in a coarsening two-dimensional XY model *Phys. Rev.* E **68** 021109
[33] Rana N and Perlekar P 2020 Coarsening in the two-dimensional incompressible Toner-Tu equation: signatures of turbulence *Phys. Rev.* E **102** 032617
[34] Rana N and Perlekar P 2022 Phase ordering, topological defects and turbulence in the three-dimensional incompressible Toner-Tu equation *Phys. Rev.* E **105** L032603
[35] Aditi Simha R and Ramaswamy S 2002 Hydrodynamic fluctuations and instabilities in ordered suspensions of self-propelled particles *Phys. Rev. Lett.* **89** 058101
[36] Dombrowski C, Cisneros L, Chatkaew S, Goldstein R E and Kessler J O 2004 Self-concentration and large-scale coherence in bacterial dynamics *Phys. Rev. Lett.* **93** 098103
[37] Ramaswamy S 2010 The mechanics and statistics of active matter *Annu. Rev. Condens. Matter Phys.* **1** 323–45
[38] Uchida N and Golestanian R 2010 Synchronization and collective dynamics in a carpet of microfluidic rotors *Phys. Rev. Lett.* **104** 178103
[39] Wensink H H, Dunkel J, Heidenreich S, Drescher K, Goldstein R E, Löwen H and Yeomans J M 2012 Meso-scale turbulence in living fluids *Proc. Natl Acad. Sci.* **109** 14308–13
[40] Chatterjee R, Rana N, Aditi Simha R, Perlekar P and Ramaswamy S 2021 Inertia drives a flocking phase transition in viscous active fluids *Phys. Rev.* X **11** 031063
[41] Rana N, Chatterjee R, Ro S, Levine D, Ramaswamy S and Perlekar P 2024 Defect turbulence in a dense suspension of polar, active swimmers *Phys. Rev.* E **109** 024603
[42] Sanchez T, Chen D T N, DeCamp S J, Heymann M and Dogic Z 2012 Spontaneous motion in hierarchically assembled active matter *Nature* **491** 431–4
[43] Giomi L, Bowick M J, Ma X and Marchetti M C 2013 Defect annihilation and proliferation in active nematics *Phys. Rev. Lett.* **110** 228101
[44] Thampi S P, Golestanian R and Yeomans J M 2013 Velocity correlations in an active nematic *Phys. Rev. Lett.* **111** 118101
[45] Martínez-Prat B, Alert R, Meng F, Ignés-Mullol J, Joanny J-F, Casademunt J, Golestanian R and Sagués F 2021 Scaling regimes of active turbulence with external dissipation *Phys. Rev.* X **11** 031065
[46] Kawaguchi K, Kageyama R and Sano M 2017 Topological defects control collective dynamics in neural progenitor cell cultures *Nature* **545** 327–31
[47] Saw T B, Doostmohammadi A, Nier V, Kocgozlu L, Thampi S, Toyama Y, Marcq P, Lim C T, Yeomans J M and Ladoux B 2017 Topological defects in epithelia govern cell death and extrusion *Nature* **544** 212–6
[48] Maroudas-Sacks Y, Garion L, Shani-Zerbib L, Livshits A, Braun E and Keren K 2020 Topological defects in the nematic order of actin fibres as organization centres of hydra morphogenesis *Nat. Phys.* **17** 251–9
[49] Copenhagen K, Alert R, Wingreen N S and Shaevitz J W 2021 Topological defects promote layer formation in *Myxococcus xanthus* colonies *Nat. Phys.* **17** 211–5
[50] Dafermos C M 1970 Disinclinations in liquid crystals *Q. J. Mech. Appl. Math.* **23** 49–64
[51] Imura H and Okano K 1973 Friction coefficient for a moving disinclination in a nematic liquid crystal *Phys. Lett.* A **42** 403–4
[52] Eshelby J D 1980 The force on a disclination in a liquid crystal *Phil. Mag.* A **42** 359–67
[53] Ambegaokar V, Halperin B I, Nelson D R and Siggia E D 1980 Dynamics of superfluid films *Phys. Rev.* B **21** 1806–26
[54] Dubois-violette E, Guazzelli E and Prost J 1983 Dislocation motion in layered structures *Phil. Mag.* A **48** 727–47
[55] Kawasaki K 1983 Variational approach to dynamics of interfaces and quantized vortex lines *Physica* A **119** 17–40
[56] Kawasaki K 1984 Topological defects and non-equilibrium *Prog. Theor. Phys. Supp.* **79** 161–90
[57] Kawasaki K 1984 Dynamical theory of topological defects *Ann. Phys., NY* **154** 319–55
[58] Bodenschatz E, Pesch W and Kramer L 1988 Structure and dynamics of dislocations in an anisotropic pattern-forming systems *Physica* D **32** 135–45
[59] Neu J C 1990 Vortices in complex scalar fields *Physica* D **43** 385–406
[60] Pismen L M and Rodriguez J D 1990 Mobility of singularities in the dissipative Ginzburg-Landau equation *Phys. Rev.* A **42** 2471–4
[61] Rubinstein J 1991 Self-induced motion of line defects *Q. Appl. Math.* **49** 1–9
[62] Rodriguez J D, Pismen L M and Sirovich L 1991 Motion of interacting defects in the Ginzburg-Landau model *Phys. Rev.* A **44** 7980–4
[63] Pismen L M and Rubinstein J 1991 Motion of vortex lines in the Ginzburg-Landau model *Physica* D **47** 353–60
[64] Denniston C 1996 Disclination dynamics in nematic liquid crystals *Phys. Rev.* B **54** 6272–5
[65] Pleiner H 1988 Dynamics of a disclination point in smectic-C and -C* liquid-crystal films *Phys. Rev.* A **37** 3986–92
[66] Semenov A N 1999 Interaction of point defects in a nematic liquid *Europhys. Lett.* **46** 631
[67] Najafi A and Golestanian R 2003 Phonon-mediated anomalous dynamics of defects *Eur. Phys. J.* B **34** 99–103

[68] Radzihovsky L 2015 Anomalous energetics and dynamics of moving vortices *Phys. Rev. Lett.* **115** 247801
[69] Kruse K, Joanny J F, Jülicher F, Prost J and Sekimoto K 2004 Asters, vortices and rotating spirals in active gels of polar filaments *Phys. Rev. Lett.* **92** 078101
[70] Pismen L M 2013 Dynamics of defects in an active nematic layer *Phys. Rev.* E **88** 050502
[71] Tang X and Selinger J V 2019 Theory of defect motion in 2D passive and active nematic liquid crystals *Soft Matter* **15** 587–601
[72] Cortese D, Eggers J and Liverpool T B 2018 Pair creation, motion and annihilation of topological defects in two-dimensional nematic liquid crystals *Phys. Rev.* E **97** 022704
[73] Vafa F, Bowick M J, Marchetti M C and Shraiman B I 2020 Multi-defect dynamics in active nematics (arXiv:2007.02947)
[74] Zhang Y-H, Deserno M and Tu Z-C 2020 Dynamics of active nematic defects on the surface of a sphere *Phys. Rev.* E **102** 012607
[75] Angheluta L, Chen Z, Marchetti M C and Bowick M J 2021 The role of fluid flow in the dynamics of active nematic defects *New J. Phys.* **23** 033009
[76] Vafa F 2022 Defect dynamics in active polar fluids vs. active nematics *Soft Matter* **18** 8087–97
[77] Aranson I S, Kramer L and Weber A 1991 On the interaction of spiral waves in non-equilibrium media *Physica* D **53** 376–84
[78] Aranson I S, Kramer L and Weber A 1993 Theory of interaction and bound states of spiral waves in oscillatory media *Phys. Rev.* E **47** 3231–41
[79] Aranson I S and Kramer L 2002 The world of the complex Ginzburg-Landau equation *Rev. Mod. Phys.* **74** 99–143
[80] Pismen L M and Nepomnyashchy A A 1992 On interaction of spiral waves *Physica* D **54** 183–93
[81] Pisegna G, Saha S and Golestanian R 2024 Emergent polar order in non-polar mixtures with non-reciprocal interactions (arXiv:2404.05396)
[82] Hagan P S 1982 Spiral waves in reaction-diffusion equations *SIAM J. Appl. Math.* **42** 762–86
[83] Hendrey M, Nam K, Guzdar P and Ott E 2000 Target waves in the complex Ginzburg-Landau equation *Phys. Rev.* E **62** 7627–31
[84] Cox S M and Matthews P C 2002 Exponential time differencing for stiff systems *J. Comput. Phys.* **176** 430–55
[85] Berg B and Lüscher M 1981 Definition and statistical distributions of a topological number in the lattice O(3) σ-model *Nucl. Phys.* B **190** 412–24
[86] Bohr T, Huber G and Ott E 1997 The structure of spiral-domain patterns and shocks in the 2D complex Ginzburg-Landau equation *Physica* D **106** 95–112
[87] Brito C, Aranson I S and Chaté H 2003 Vortex glass and vortex liquid in oscillatory media *Phys. Rev. Lett.* **90** 068301